

MIT Open Access Articles

Probing nanoparticle translocation across the permeable endothelium in experimental atherosclerosis

The MIT Faculty has made this article openly available. **Please share** how this access benefits you. Your story matters.

Citation: Kim, Y., M. E. Lobatto, T. Kawahara, B. Lee Chung, A. J. Mieszawska, B. L. Sanchez-Gaytan, F. Fay, et al. "Probing Nanoparticle Translocation Across the Permeable Endothelium in Experimental Atherosclerosis." *Proceedings of the National Academy of Sciences* 111, no. 3 (January 21, 2014): 1078–1083.

As Published: <http://dx.doi.org/10.1073/pnas.1322725111>

Publisher: National Academy of Sciences (U.S.)

Persistent URL: <http://hdl.handle.net/1721.1/89112>

Version: Final published version: final published article, as it appeared in a journal, conference proceedings, or other formally published context

Terms of Use: Article is made available in accordance with the publisher's policy and may be subject to US copyright law. Please refer to the publisher's site for terms of use.



Probing nanoparticle translocation across the permeable endothelium in experimental atherosclerosis

YongTae Kim^{a,1}, Mark E. Lobatto^{b,c,1}, Tomohiro Kawahara^d, Bomy Lee Chung^{e,f}, Aneta J. Mieszawska^b, Brenda L. Sanchez-Gaytan^b, Francois Fay^b, Max L. Senders^b, Claudia Calcagno^b, Jacob Becraft^g, May Tun Saung^h, Ronald E. Gordonⁱ, Erik S. G. Stroes^c, Mingming Ma^e, Omid C. Farokhzad^j, Zahi A. Fayad^b, Willem J. M. Mulder^{b,c,2}, and Robert Langer^{e,f,g,k,2}

^aThe George W. Woodruff School of Mechanical Engineering, Institute for Electronics and Nanotechnology, Parker H. Petit Institute for Bioengineering and Bioscience, Georgia Institute of Technology, Atlanta, GA 30332; ^bTranslational and Molecular Imaging Institute, Icahn School of Medicine at Mount Sinai, New York, NY 10029; ^cDepartment of Vascular Medicine, Academic Medical Center, 1105 AZ, Amsterdam, The Netherlands; ^dDepartment of Biological Functions and Engineering, Kyushu Institute of Technology, Fukuoka 804-8550, Japan; ^eDavid H. Koch Institute for Integrative Cancer Research, ^fDepartment of Chemical Engineering, ^gDepartment of Biological Engineering, and ^hHarvard-MIT Division of Health Sciences and Technology, Massachusetts Institute of Technology, Cambridge, MA 02139; ⁱBoston University School of Medicine, Boston, MA 02215; ^jDepartment of Pathology, Mount Sinai Hospital, New York, NY 10029; and ^kDepartment of Anesthesiology, Brigham and Women's Hospital, Harvard Medical School, Boston, MA 02215

Contributed by Robert Langer, December 6, 2013 (sent for review November 6, 2013)

Therapeutic and diagnostic nanomaterials are being intensely studied for several diseases, including cancer and atherosclerosis. However, the exact mechanism by which nanomedicines accumulate at targeted sites remains a topic of investigation, especially in the context of atherosclerotic disease. Models to accurately predict transvascular permeation of nanomedicines are needed to aid in design optimization. Here we show that an endothelialized microchip with controllable permeability can be used to probe nanoparticle translocation across an endothelial cell layer. To validate our in vitro model, we studied nanoparticle translocation in an in vivo rabbit model of atherosclerosis using a variety of preclinical and clinical imaging methods. Our results reveal that the translocation of lipid-polymer hybrid nanoparticles across the atherosclerotic endothelium is dependent on microvascular permeability. These results were mimicked with our microfluidic chip, demonstrating the potential utility of the model system.

nanotechnology | cardiovascular disease | microfluidics | noninvasive imaging

Improving the design of nanomedicines is key for their success and ultimate clinical application (1). The accumulation of such therapeutic or diagnostic nanomaterials primarily relies on enhanced endothelial permeability of the microvasculature in diseased tissue (2). This holds true for a wide range of pathological conditions, including inflammation, atherosclerosis, and most notably, oncological disease (3–6). Although attributed to the enhanced permeability and retention (EPR) effect, the exact mechanism by which nanoparticles accumulate in tumors continues to be a topic of research (7, 8). The “leaky” vasculature of tumors, which facilitates the extravasation of nanoparticles from microvessels (9), is a heterogeneous phenomenon that varies between different tumor models and even more so in patients. Moreover, the exploitation of nanomedicines in other conditions with enhanced microvessel permeability has only recently begun to be studied in detail. For example, in the last 5 y, a small but increasing number of preclinical studies that apply nanoparticle therapy in atherosclerosis models has surfaced (10). Although several targeting mechanisms have been proposed (4), the exact mechanism by which nanoparticles accumulate in atherosclerotic plaques remains to be investigated, but is likely facilitated by highly permeable neovessels that penetrate into the plaque from the vasa vasorum (Fig. 1A), a network of microvessels that supplies the wall of larger vessels (11).

Advances in biomedical imaging allow the study of plaque-targeting nanoparticles in a dynamic fashion with exceptional

detail (12, 13). Microchip technology has the potential to monitor nanoparticle behavior at the (sub)cellular level. Microfluidic chips in which endothelial cells (ECs) are grown in the channels can serve as unique in vitro test systems to study microvascular function and associated disorders (14–18). They allow the isolation of specific biological hallmarks relevant to nanoparticle accumulation, such as the leaky endothelium. In the current study, we validate the potential utility of our microchip technology to study nanoparticle translocation over the endothelium and combine this with in vivo and ex vivo multimodality imaging studies on a rabbit model to better understand nanoparticle targeting of atherosclerotic plaques.

Results and Discussion

We developed an endothelialized microfluidic device where the two-layer microfluidic channels are compartmentalized, which enables independent flow modulation in each channel and supply of controlled shear stress and stimuli to the cells (Fig. 1B) (19). To monitor permeability, we installed four electrodes into the inlet and outlet of the upper and lower channels and measured the transendothelial electrical resistance (TEER) across the endothelial layer (Fig. 1C; for details on device fabrication,

Significance

This study shows that an endothelialized microfluidic chip with controllable permeability can serve as a model for nanoparticle translocation across the permeable endothelium. Integration of this in vitro model and an in vivo rabbit model revealed that the extravasation of nanoparticles across the endothelium in atherosclerotic plaques depends on microvascular permeability. This approach represents a unique method for the assessment of nanoparticle behavior across the atherosclerotic endothelium, and may also serve as a valuable tool to study nanomedicine accumulation in a variety of other diseases.

Author contributions: Y.K., M.E.L., W.J.M.M., and R.L. designed research; Y.K., M.E.L., T.K., B.L.C., A.J.M., B.L.S.-G., F.F., M.L.S., C.C., J.B., and M.T.S. performed research; Y.K., M.E.L., T.K., B.L.C., A.J.M., B.L.S.-G., R.E.G., E.S.G.S., M.M., O.C.F., Z.A.F., W.J.M.M., and R.L. contributed new reagents/analytic tools; Y.K., M.E.L., T.K., O.C.F., Z.A.F., W.J.M.M., and R.L. analyzed data; and Y.K., M.E.L., W.J.M.M., and R.L. wrote the paper.

The authors declare no conflict of interest.

¹Y.K. and M.E.L. contributed equally to this work.

²To whom correspondence may be addressed. E-mail: rlander@mit.edu or Willem.Mulder@mssm.edu.

This article contains supporting information online at www.pnas.org/lookup/suppl/doi:10.1073/pnas.1322725111/-DCSupplemental.

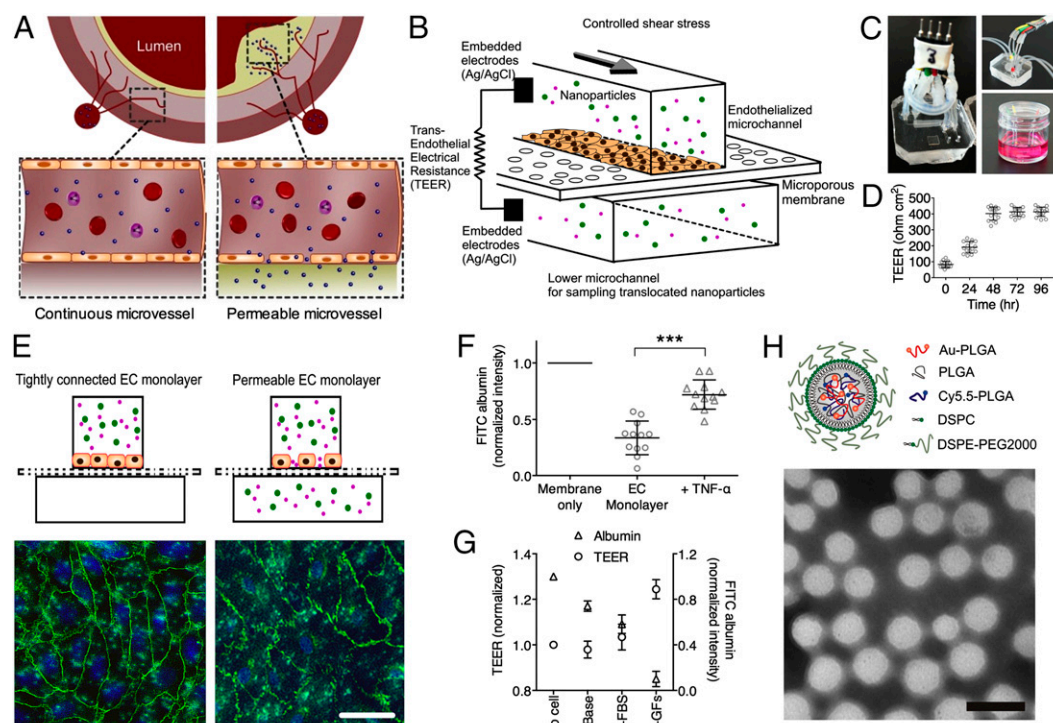


Fig. 1. Development of an endothelialized microfluidic device to probe nanoparticle translocation over a permeable microvessel. (A) Schematics of continuous normal capillaries surrounding the vessel wall as well as permeable capillaries that penetrate into the atherosclerotic plaque from the vasa vasorum. (B) Schematic of an endothelialized microfluidic device that consists of two-layer microfluidic channels that are separated by a porous membrane (3 μm pore) on which ECs are grown. (C) TEER was dynamically measured across the endothelial layer on the membrane between the upper and lower channels. (D) A well-established monolayer of the microvascular endothelium is formed at TEER ~ 400 ($\Omega\cdot\text{cm}^2$). (E) The monolayer becomes highly permeable when stimulated with the inflammatory mediator, TNF- α , as well as with shear stress, with disruption of intercellular junctional structures (i.e., adherens junctions) between ECs, as evidenced by patchy expression of VE-cadherin (green) in the image on the right versus the left. Blue depicts nuclei stained with DAPI. (Scale bar, 20 μm .) (F) FITC-albumin translocation through the endothelial monolayer increases when the chip is treated with TNF- α . (G) The chip with endothelium cultured in different culture media [base, +FBS, +growth factors (GFs)] for 6 h shows a decrease in TEER with increased FITC-albumin translocation. No cell indicates the membrane only. TEER was normalized to the level with no cells (membrane only). (H) Schematic and TEM image of PEGylated lipid-coated nanoparticles encapsulating PLGA-conjugated AuNCs and Cy5.5. The average size was 69.7 ± 14 nm, which was measured from TEM images. (Scale bar, 100 nm.) Details on labeling, synthesis, characterization, and large-scale production procedures can be found in *Materials and Methods* and Fig. S2.

see *Materials and Methods* and Fig. S1). Long-term culture of ECs with growth factors in the device produced a well-established endothelial monolayer with a TEER greater than 400 ($\Omega\cdot\text{cm}^2$) (Fig. 1D), which we independently corroborated with fluorescence microscopy (Fig. 1E). Systemic inflammation is known to play a pivotal role in endothelial dysfunction and the progression of atherosclerosis. Tumor necrosis factor α (TNF- α), an inflammatory cytokine with a wide range of proinflammatory activities, is involved in the pathogenesis of atherosclerosis and causes vascular dysfunction (20). Elevated levels of TNF- α in plasma are associated with cardiovascular risk (21). The plasma concentration of TNF- α in patients with coronary artery disease was found to be 21 ng/mL (22). When media with TNF- α (20 ng/mL) were infused into the microfluidic chip, this resulted in disrupted intercellular junctions (e.g., adherens junctions) and associated increased endothelial permeability (Fig. 1E). This was verified by increased translocation of FITC-labeled albumin, an endothelial permeability marker (Fig. 1F). We observed variations in TEER and albumin translocation under different cell culture media conditions (Fig. 1G). To study nanoparticle translocation, we designed and scaled up the production of a lipid-polymer hybrid nanoparticle that was labeled with gold nanocrystals (AuNCs) and the near infrared fluorescent (NIRF) dye Cy5.5 to allow its detection by transmission electron microscopy (TEM) and NIRF imaging, respectively (Fig. 1H and Fig. S2) (23, 24).

Before nanoparticles were applied, we also studied the influence of shear stresses on endothelial permeability within the microfluidics device as hemodynamic forces can alter the function of ECs (25). Although shear stress (>15 dyne/cm 2) is a prerequisite to quiescent ECs and to align them in the direction of arterial blood flow, low shear stress (<4 dyne/cm 2) stimulates the development of atherosclerosis (26). In our study, the endothelial monolayer showed a reduction in TEER (i.e., an increase in permeability) when cells were stimulated by shear stresses (1 and 10 dyne/cm 2) (Fig. 2A). Additional stimulation with TNF- α (20 ng/mL) for 90 min led to a further increase in permeability, which could be altered by varying shear stress levels. The changes in permeability could be sustained for an additional 90 min, as indicated by the decreased TEER (Fig. 2B). After 90 min of TNF- α stimulation and another 90 min of relaxation, TEER remained stable for at least another 60 min (Fig. 2C). In addition, we note that the pressure differential across the endothelial layer in the chip can be modulated to, for example, mimic the high interstitial pressure of tumors (19).

Subsequently, we infused lipid-polymer hybrid nanoparticles in the device for 1 h and probed their translocation. The fluorescent intensity of the nanoparticles sampled from the lower channel every 10 min was $\sim 4\text{--}5\%$ of the initial intensity in the upper channel (Fig. 2D). Importantly, we found a significant increase of nanoparticle translocation across the endothelium when cells were treated with TNF- α and TEER decreased (Fig. 2E). Notably, a linear regression analysis showed a significant correlation

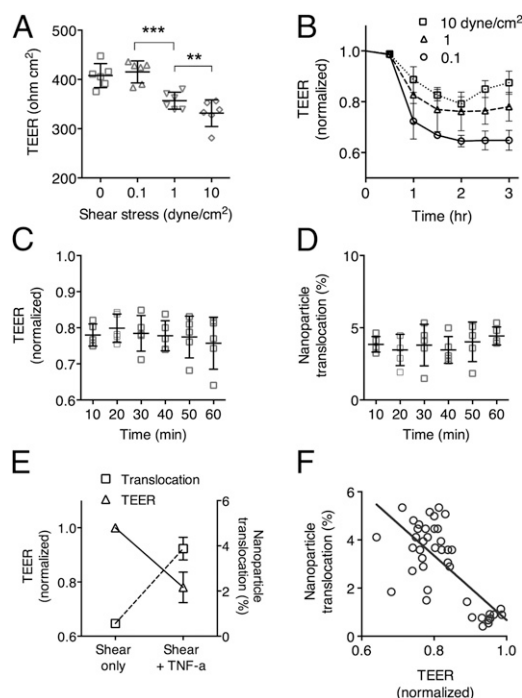


Fig. 2. Chip modulation, the monitoring of endothelial permeability, and nanoparticle translocation. (A) EC monolayers show an increase in permeability (i.e., a decrease in TEER) when ECs are exposed to shear stresses (1 and 10 dyne/cm²) for 24 h. (B) Stimulation with TNF- α (20 ng/mL) for 1.5 h leads to an increase in permeability (i.e., a decrease in TEER) for 3 h (with no treatment for 1.5 h). Lower shear stress shows the greatest increase in permeability in combination with TNF- α . TEER values are normalized at the beginning of TNF- α stimulation after 24 h of shear stress of 1 dyne/cm². The error bar is SEM ($n = 3$). (C) Variation of TEER over a 1 h time span, after 90 min of TNF- α stimulation followed by 90 min relaxation for 3 h in B. (D) Nanoparticle translocation is $\sim 4\%$ after stimulation with TNF- α . For calculation of nanoparticle translocation, see *Materials and Methods*. (E) Stimulation with TNF- α , in addition to shear stress of 1 dyne/cm², increases nanoparticle translocation. The error bar is SD ($n = 5$). (F) Nanoparticle translocation and TEER are inversely correlated ($r^2 = 0.54$, $P < 0.0001$).

($P < 0.0001$) between nanoparticle translocation and permeability as measured with TEER (Fig. 2F).

To compare endothelial permeability of the endothelialized microfluidic chips with an *in vivo* atherosclerosis model, we used New Zealand White (NZW) rabbits that underwent a double balloon injury of the aorta and were fed a high-cholesterol diet, a well-established method to induce atherosclerotic lesions (27). These lesions have an abundance of neovessels that originate from the vasa vasorum within the adventitia of the vessel wall that can reach into the atherosclerotic plaque (Fig. S3). NZW rabbits that were fed a chow diet served as a healthy control group. We set up both *in vivo* and *ex vivo* imaging protocols (for details, see *Materials and Methods*) to investigate endothelial permeability of the entire aortic abdominal vessel wall.

A 3D dynamic contrast enhanced magnetic resonance imaging (3D DCE-MRI) technique was used to probe atherosclerotic plaque microvessel permeability *in vivo* on a 3 tesla clinical MRI scanner. We observed a clear difference in vascular permeability between control and atherosclerotic rabbits (Fig. 3A), which is exemplified by the multiple red regions along the aorta of the atherosclerotic rabbit. We consequently validated the *in vivo* DCE-MRI results with *ex vivo* albumin-enhanced NIRF imaging of intact aortas. Similar to the experiments performed with the microfluidic device, albumin served as a tracer for vascular permeability. We observed a significant difference between the

permeability of control and atherosclerotic aortas, confirming marked endothelial permeability in the atherosclerosis model (Fig. 3B). Linear regression analysis showed a significant degree of correlation between the *in vivo* DCE-MRI and *ex vivo* permeability measures (Fig. 3C). To show the difference of the endothelial lining of the vessel wall at high resolution at microscopic levels, we performed TEM of ultrathin sliced sections (1 μm) of the excised aortas (Fig. 3D). The normal vessel wall was completely covered by an endothelial layer with tight interendothelial junctions, whereas the endothelial lining of the atherosclerotic vessel wall showed large paracellular gaps, which can potentially permit extravasation of macromolecules and cells (28).

NIRF imaging was used to compare nanoparticle and albumin translocation in both the endothelialized microfluidic chip and the rabbit model of atherosclerosis. To this end, we prepared endothelialized microfluidic chips, subjected them to shear stress at 1 dyne/cm², and perfused them with either saline or TNF- α in pairs. Subsequently, the Cy5.5- and gold-labeled nanoparticles and Cy7-labeled albumin were perfused through the upper channel of the

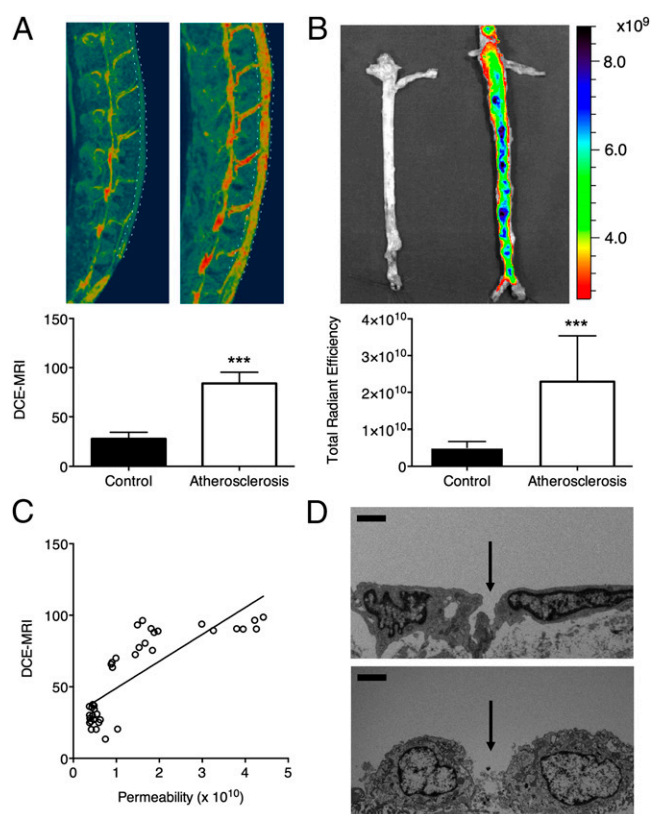
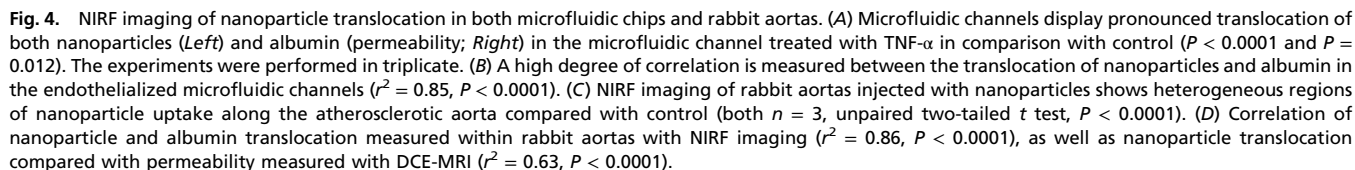
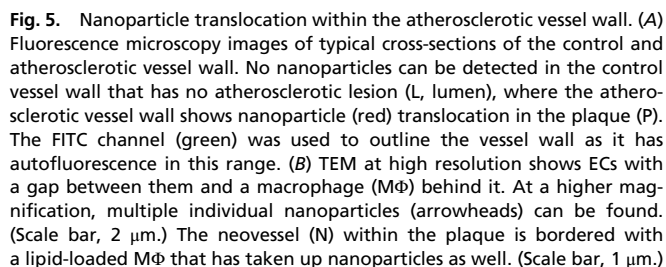


Fig. 3. Endothelial permeability of a rabbit model of atherosclerosis evaluated by imaging. (A) Sagittal *in vivo* 3D DCE-MRI maps of a control rabbit (Left) versus a rabbit with atherosclerosis (Right); the aortas are centered between the white dashed lines. The red regions indicate the areas of increased permeability (both $n = 3$, unpaired two-tailed t test, $P < 0.0001$). (B) *Ex vivo* NIRF imaging of excised aortas of rabbits injected with Cy7-albumin, a marker for permeability, showing permeability of the vessel wall of atherosclerotic rabbits (Right) compared with control animals (Left) (both $n = 3$, unpaired two-tailed t test, $P < 0.0001$). (C) Correlation of *in vivo* and *ex vivo* measures of permeability, 3D DCE-MRI, and Cy7-labeled NIRF imaging, showing a high degree of correlation between both imaging modalities ($r^2 = 0.65$, $P < 0.0001$). (D) TEM of the endothelial lining of the vessel wall of both a control and an atherosclerotic rabbit showing tight adherent endothelial junctions in the control rabbit, while the atherosclerotic vessel wall has a large gap between ECs. (Scale bar, 2 μm .) For DCE-MRI, the IAUC after 2 min was used. NIRF imaging is expressed in total radiant efficiency in [p/s]/[$\mu\text{W}/\text{cm}^2$].



fashion and therefore serves as a complementary *in vitro* model to screen nanoparticles and optimize their design. A limitation of the current study is that we did not screen for different particle sizes. Nevertheless, the translocation of the nanoparticle, which was of a therapeutically relevant size, correlated well with albumin-based permeability measures. Importantly, the same correlation between albumin deposition and nanoparticle accumulation was



found in atherosclerotic aortas harvested from a rabbit model. An in-depth fluorescence and electron microscopy investigation revealed that these nanoparticles were deposited in vesicles of atherosclerotic plaque macrophages, in the proximity of disrupted endothelium, at both the luminal side of the plaque and microvessels in the adventitia that originate from the vasa vasorum (29).

The data demonstrate that nanoparticle translocation for plaque targeting occurs at sites of increased permeability, via the luminal and adventitial side of the arterial wall, providing good accessibility for nanomedicines to an atherosclerotic plaque. The integration of multimodality imaging revealed the similarities between the rabbit data and the *in vitro* model, which signifies that the microfluidic system can serve as a unique tool to examine nanoparticle translocation over microvessels. This integrative approach can be applied to optimize nanoparticle design and to study the potential of nanomedicine in the context of a range of other diseases, including cancer, diabetes, and inflammation.

Materials and Methods

Microfluidic Device Design and Fabrication. The upper and lower channels were fabricated with polydimethylsiloxane (PDMS) (SYLGARD 184, Dow Corning) using standard soft-lithography techniques (30). The upper channel is 200 μm wide and 200 μm tall, and the lower channel is 400 μm wide and 200 μm tall. We installed the electrodes into the upper channel before bonding the two PDMS slabs with a microporous polyester membrane (CLS3452, Sigma-Aldrich) treated with 3-aminopropyl-triethoxysilane (APTES) (31) to complete the device (Fig. S1).

TEER Measurement. We used commercially available voltohmmeters (EVOM, World Precision Instruments) to measure TEER. We optimized the length of the Ag/AgCl electrodes (381 μm in diameter, A-M Systems) to tune the base level resistance when they are embedded in microfluidic channels. We developed the custom connectors to fit both EVOM and our device. The unit of TEER was given by ($\text{Ohm}\cdot\text{cm}^2$) from TEER measurement (Ohm) and area of the membrane in the channel for better comparison.

Cell Culture in the Chip. Human umbilical vein ECs (HUVECs; PCS-100-013, ATCC) were maintained in vascular cell basal medium (VCBM; PCS-100-030, ATCC) supplemented with EC growth kit/VEGF (PCS-100-041, ATCC) at a pH of 7.4. The device, tubing, and other components were sterilized in 70% ethanol, washed with deionized (DI) water three times, rinsed with PBS three times, and dried in a sterilized area. The membrane was coated with 50 $\mu\text{g}/\text{mL}$ fibronectin from human plasma (F2006, Sigma Aldrich) for 1 h. We infused 100 μL of HUVECs ($>500,000$ cells/mL) into the microfluidic device and cultured them for 3–4 d.

Shear Stress Calculation. The volumetric flow rates of 0.8, 8, and 80 $\mu\text{L}/\text{min}$ give 0.33, 3.3, and 33 mm/s of fluid velocity, where the shear stresses, τ_{cell} , experienced by ECs were computed to be 0.1, 1, and 10 dyne/cm^2 , respectively (32).

Immunofluorescent Staining. Cells were fixed with 2% paraformaldehyde, rinsed with PBS containing 1% BSA, permeabilized with 0.1% Triton X-100, and then immunostained with antibodies against vascular endothelial (VE)-cadherin (goat polyclonal IgG, 200 $\mu\text{g}/\text{mL}$, Santa Cruz Biotechnology) for 40 min at room temperature. Cultures incubated with goat IgG served as negative immunofluorescent controls. After washing, fluorescent secondary antibodies (Alexa-488-conjugated donkey anti-goat at 40 $\mu\text{g}/\text{mL}$, Invitrogen, Inc.) were added for 40 min in the dark at room temperature.

FITC-Albumin Permeability Assay. The endothelial permeability in the chip was also assessed by measuring FITC-albumin translocation across the monolayer. We infused 1 mg/mL of FITC-albumin in the medium into the upper channel at a flow rate of 8 $\mu\text{L}/\text{min}$, which corresponds to a shear stress of 1 dyne/cm^2 . The translocation was determined by serially sampling the liquid continuously from the lower channel at a flow rate of 2 $\mu\text{L}/\text{min}$ for 30 min.

Nanoparticle Synthesis. We prepared and synthesized AuNCs (33), PLGA-conjugated AuNCs, PLGA-conjugated Cy5.5 Rhodamine, Cy7-modified albumin, and lipid-PLGA nanoparticles (Fig. S2; for details on the nanoparticle synthesis, see [Nanoparticle Preparation](#)).

Nanoparticle Suspension and Sampling. Lipid-polymer nanoparticles (100 $\mu\text{g}/\text{mL}$) were suspended in medium and infused into the upper channel at a flow rate of 8 $\mu\text{L}/\text{min}$, which corresponds to a shear stress of 1 dyne/cm^2 . The lower channel was serially sampled every 10 min at a flow rate of 2 $\mu\text{L}/\text{min}$ for a total of 20 μL every 10 min for 1 h. Nanoparticle translocation (%) was calculated by the ratio of fluorescent intensity of sampled nanoparticles to fluorescent intensity of suspended nanoparticles. Fluorescent intensity of the nanoparticles was measured after nanoparticle solution was diluted; that is, 20 μL were diluted five times by adding 80 μL of medium to make the total volume of 100 μL .

Animal Model. Seven NZW male rabbits were included in this study. Four animals underwent a combination of a high-fat diet and balloon angioplasties to create advanced atherosclerotic lesions after a 6-mo time frame. A detailed account of the model has been described previously (27). Six animals underwent DCE-MRI (three control and three atherosclerotic animals). For DCE-MRI, animals were anesthetized with an intramuscular injection of Ketamine and Xylazine (35 mg/kg and 5 mg/kg) and placed in the MRI under Isoflurane anesthesia at 1.5%, whereas vital parameters were monitored. Animals were killed by an overdose of 100 mg/kg sodium pentobarbital. All *i.v.* injections (Gadolinium, nanoparticles, Cy7-albumin, sodium pentobarbital) were administered through a 22 G catheter that was placed in the marginal ear vein. Before excision of the aortas, the rabbits were perfused with heparinized saline to clear the vasculature of blood. Aortas were measured in length, marked with sutures, and consequently harvested from the superior mesenteric artery to the iliac bifurcation. The complete excised vessel was imaged with NIRF imaging. All animal experiments were approved by the Institutional Animal Care and Use Committee at the Icahn School of Medicine at Mount Sinai.

3D DCE-MRI. A 3D DCE-MRI was performed on a 3 T whole-body scanner (Philips Achieva) with a product 8 channels knee coil. The abdominal aorta was localized with scout scans and a time of flight noncontrast enhanced angiography. Gadolinium (gadopentetate dimeglumine, Magnevist, Bayer Healthcare) was injected during a 3D turbo field echo sequence with motion-sensitized driven equilibrium preparation for black blood imaging. The sequence covered the aorta from the right renal artery to the iliac bifurcation. Imaging parameters were set at the following: relaxation time (TR), 6.2 ms; echo time (TE), 2.8 ms; flip angle, 20 degrees; echo train length (ETL), 80; spatial resolution, 0.6 mm^3 ; field of view (FOV), 160 mm^2 ; 20 slices; orientation, sagittal. Images were acquired before, during, and up to 10 min after contrast agent injection to quantify permeability of the vessel wall (acquisition with three signal averages; time resolution, 32 s).

NIRF Imaging. A Xenogen IVIS-200 optical imaging system was used for NIRF imaging. Filters for imaging of the microfluidic device and imaging of excised aortas were set at 675–720 nm for detection of Cy5.5 and 745–800 nm for detection of Cy7. The exposure time for the microfluidic device was set at 40 s, binning at 4, and FOV of 6.5 cm. For the aortas, the exposure times were set at 5 and 2 s for Cy5.5 and Cy7 imaging, respectively, with binning at 4 and a FOV of 22.8 cm.

Analyses of Imaging Data. In 3D DCE-MRI, the inner and outer walls of the aortas were traced on 162 ± 8 contiguous axially reformatted slices ranging from the left renal artery to the iliac bifurcation in OsiriX 5.6 (Pixmeo). The vessel wall contours were consequently superimposed to initial area under the curve (IAUC) parametric maps to calculate the under-the-contrast agent time curves for the average IAUC in the vessel wall of each traced axial slice. The IAUCs after 2 min were calculated with custom-built Matlab software and used as time point for data analysis. In the NIRF data analysis of the endothelialized microfluidic chips, six parallel regions of interest (ROIs) of 0.2 cm were placed, thereby covering the full channel. The ROIs were consequently copied and placed on the alternative wavelength. Total radiant efficiency [$\text{p/s}/[\mu\text{W}/\text{cm}^2]$] was used for data analysis. For the excised aortas, ROIs of 1 cm were placed over the vessel wall, starting at the left renal artery down to the iliac bifurcation. According to aortic lengths, six or seven ROIs were placed. Similar to the microfluidic chips, the ROIs for one wavelength were transferred to the other. In the DCE analysis and DCE to NIRF image comparison, the IAUC 2 of the DCE data were divided into six or seven sections, according to the length of the aorta. The sum of the IAUC 2 in those regions was used for data analysis. Linear regression was calculated by matching the respective NIRF and DCE sections.

Fluorescence Microscopy. After NIRF imaging, the part of the aorta below the left renal aorta was transversely cut into 0.5 cm sections and embedded in

optimal cutting temperature compound blocks and stored at -80°C . The blocks were sectioned in $5\text{ }\mu\text{m}$ sections and mounted on slides with Vecta-mount (DAKO). Fluorescence microscopy was performed on a Zeiss AxioPlan 2 microscope with a Cy5 filter for the detection of nanoparticles.

TEM. TEM images were acquired using a Hitachi 7650 TEM operated at 80 kV coupled to a Scientific Instruments and Applications digital camera controlled by Maxim CCD software. For the nanoparticle imaging, the nanoparticle solution was negatively stained with a 2% phosphotungstic acid solution. Then, a $10\text{ }\mu\text{L}$ solution of nanoparticles was cast on a 100 mesh Formvar coated nickel grid (Electron Microscopy Sciences), air-dried, and imaged. For the animal model imaging, aortic rings of 0.5 cm were cut below the celiac artery immediately after sacrifice and stored in 3.0% glutaraldehyde in 0.2 M sodium cacodylate as a buffer in pH 7.4. The rings were washed in buffer and treated with osmium tetroxide 1% for 1 h and dehydrated in graded steps of ethanol, cleared with propylene oxide, and embedded in EMbed 812 (Electron Microscopy Sciences). Ultrathin sections were cut and mounted on a grid for imaging.

Histology. Additional aortic rings were cut for conventional histology and placed in 4% paraformaldehyde. The rings were embedded in paraffin 24 h later and cut into sections of $5\text{ }\mu\text{m}$ thickness. CD-31 stain (Dako) for ECs was applied with methods described previously (34). Images were acquired with a Philips Digital Pathology scanner.

Statistics. Paired t tests were used for the comparison of endothelialized microfluidic chips with optical imaging. Unpaired t tests were used for data analysis of the other microfluidic devices and analyses of the aortas. Linear regression was used for the correlative measures. Data are reported as mean \pm SD. P values < 0.05 were considered statistically significant.

ACKNOWLEDGMENTS. We thank the Institute for Electronics and Nanotechnology and the Petit Institute for Bioengineering and Bioscience at Georgia Institute of Technology. We thank the Microscopy Shared Resource Facility of Icahn School of Medicine at Mount Sinai for the use of fluorescent microscope, which is supported with funding from a National Institutes of Health (NIH)–National Cancer Institute shared resources grant (5R24 CA095823-04), a National Science Foundation Major Research Instrumentation grant (DBI-9724504), and an NIH shared instrumentation grant (1 S10 RR0 9145-01). This work was supported by the National Heart, Lung, and Blood Institute, NIH, as a Program of Excellence in Nanotechnology Award, Contract HHSN268201000045C (to Z.A.F. and R.L.); the National Cancer Institute Grant CA151884 (to R.L. and O.C.F.); the David H. Koch Prostate Cancer Foundation Award in Nanotherapeutics (to R.L. and O.C.F.); NIH Grants R01 EB009638 (to Z.A.F.) and R01CA155432 (to W.J.M.M.); a European Framework Program 7 Grant (to E.S.G.S.) (FP7-Health 309820: Nano-Athero); Netherlands Organization for Scientific Research ZonMW Vidi 91713324 (to W.J.M.M.); the Dutch Network for Nanotechnology NanoNext NL in the subprogram Drug Delivery; as well as the International Atherosclerosis Society and the Foundation “De Drie Lichten” in the Netherlands (to M.E.L.).

- Petros RA, DeSimone JM (2010) Strategies in the design of nanoparticles for therapeutic applications. *Nat Rev Drug Discov* 9(8):615–627.
- Farokhzad OC, Langer R (2009) Impact of nanotechnology on drug delivery. *ACS Nano* 3(1):16–20.
- Crielaard BJ, Lammers T, Schiffelers RM, Storm G (2012) Drug targeting systems for inflammatory disease: One for all, all for one. *J Control Release* 161(2):225–234.
- Lobatto ME, Fuster V, Fayad ZA, Mulder WJ (2011) Perspectives and opportunities for nanomedicine in the management of atherosclerosis. *Nat Rev Drug Discov* 10(11):835–852.
- Peer D, et al. (2007) Nanocarriers as an emerging platform for cancer therapy. *Nat Nanotechnol* 2(12):751–760.
- Schroeder A, et al. (2012) Treating metastatic cancer with nanotechnology. *Nat Rev Cancer* 12(1):39–50.
- Prabhakar U, et al. (2013) Challenges and key considerations of the enhanced permeability and retention effect for nanomedicine drug delivery in oncology. *Cancer Res* 73(8):2412–2417.
- Chauhan VP, et al. (2012) Normalization of tumour blood vessels improves the delivery of nanomedicines in a size-dependent manner. *Nat Nanotechnol* 7(6):383–388.
- Danquah MK, Zhang XA, Mahato RI (2011) Extravasation of polymeric nanomedicines across tumor vasculature. *Adv Drug Deliv Rev* 63(8):623–639.
- Godin B, et al. (2010) Emerging applications of nanomedicine for the diagnosis and treatment of cardiovascular diseases. *Trends Pharmacol Sci* 31(5):199–205.
- Granada JF, Feinstein SB (2008) Imaging of the vasa vasorum. *Nat Clin Pract Cardiovasc Med* 5(Suppl 2):S18–S25.
- Sanhai WR, Sakamoto JH, Canady R, Ferrari M (2008) Seven challenges for nanomedicine. *Nat Nanotechnol* 3(5):242–244.
- Sanz J, Fayad ZA (2008) Imaging of atherosclerotic cardiovascular disease. *Nature* 451(7181):953–957.
- Nguyen DH, et al. (2013) Biomimetic model to reconstitute angiogenic sprouting morphogenesis in vitro. *Proc Natl Acad Sci USA* 110(17):6712–6717.
- Bischel LL, Young EW, Mader BR, Beebe DJ (2013) Tubeless microfluidic angiogenesis assay with three-dimensional endothelial-lined microvessels. *Biomaterials* 34(5):1471–1477.
- Zheng Y, et al. (2012) In vitro microvessels for the study of angiogenesis and thrombosis. *Proc Natl Acad Sci USA* 109(24):9342–9347.
- Borenstein JT, et al. (2010) Functional endothelialized microvascular networks with circular cross-sections in a tissue culture substrate. *Biomed Microdevices* 12(1):71–79.
- Tsai M, et al. (2012) In vitro modeling of the microvascular occlusion and thrombosis that occur in hematologic diseases using microfluidic technology. *J Clin Invest* 122(1):408–418.
- Ernsting MJ, Murakami M, Roy A, Li SD (2013) Factors controlling the pharmacokinetics, biodistribution and intratumoral penetration of nanoparticles. *J Control Release* 172(3):782–794.
- Kleinbongard P, Heusch G, Schulz R (2010) TNF α in atherosclerosis, myocardial ischemia/reperfusion and heart failure. *Pharmacol Ther* 127(3):295–314.
- Sattar N, McCarey DW, Capell H, McInnes IB (2003) Explaining how “high-grade” systemic inflammation accelerates vascular risk in rheumatoid arthritis. *Circulation* 108(24):2957–2963.
- Schlitt A, et al. (2004) CD14+CD16+ monocytes in coronary artery disease and their relationship to serum TNF- α levels. *Thromb Haemost* 92(2):419–424.
- Kim Y, et al. (2012) Mass production and size control of lipid-polymer hybrid nanoparticles through controlled microvortices. *Nano Lett* 12(7):3587–3591.
- Mieszawska AJ, et al. (2013) Synthesis of polymer-lipid nanoparticles for image-guided delivery of dual modality therapy. *Bioconjug Chem* 24(9):1429–1434.
- Chiu JJ, Chien S (2011) Effects of disturbed flow on vascular endothelium: Pathophysiological basis and clinical perspectives. *Physiol Rev* 91(1):327–387.
- Malek AM, Alper SL, Izumo S (1999) Hemodynamic shear stress and its role in atherosclerosis. *JAMA* 282(21):2035–2042.
- Lobatto ME, et al. (2012) Imaging the efficacy of anti-inflammatory liposomes in a rabbit model of atherosclerosis by non-invasive imaging. *Methods Enzymol* 508:211–228.
- Tarbell JM (2010) Shear stress and the endothelial transport barrier. *Cardiovasc Res* 87(2):320–330.
- Moreno PR, Purushothaman KR, Sirol M, Levy AP, Fuster V (2006) Neovascularization in human atherosclerosis. *Circulation* 113(18):2245–2252.
- Qin D, Xia Y, Whitesides GM (2010) Soft lithography for micro- and nanoscale patterning. *Nat Protoc* 5(3):491–502.
- Aran K, Sasso LA, Kamdar N, Zahn JD (2010) Irreversible, direct bonding of nanoporous polymer membranes to PDMS or glass microdevices. *Lab Chip* 10(5):548–552.
- Khan OF, Sefton MV (2011) Endothelial cell behaviour within a microfluidic mimic of the flow channels of a modular tissue engineered construct. *Biomed Microdevices* 13(1):69–87.
- Mieszawska AJ, et al. (2012) Engineering of lipid-coated PLGA nanoparticles with a tunable payload of diagnostically active nanocrystals for medical imaging. *Chem Commun (Camb)* 48(47):5835–5837.
- Calcagno C, et al. (2008) Detection of neovessels in atherosclerotic plaques of rabbits using dynamic contrast enhanced MRI and 18F-FDG PET. *Arterioscler Thromb Vasc Biol* 28(7):1311–1317.